First quadruple-glycine bridging mono-lanthanide-substituted borotungstate hybrids

Jiancai Liu,[a] Jing Yu,[a] Qing Han,[a] Yue Wen,[a] Lijuan Chen[a,*] and Junwei Zhao[a,b,*]

[a]*Henan Key Laboratory of Polyoxometalate Chemistry, Institute of Molecular and Crystal Engineering, College of Chemistry and Chemical Engineering, Henan University, Kaifeng, Henan 475004, P. R. China*

[b]*State Key Laboratory of Structural Chemistry, Fujian Institute of Research on the Structure of Matter, Chinese Academy of Sciences, Fuzhou, Fujian 350002, P. R. China*

Electronic Supplementary Information

The structural refinement details in 1-6.

TG Analyses

Fig. S1 IR spectra of **1**–**6**, $K_8[\alpha\text{-}BW_{11}O_{39}H]\cdot 13H_2O$ ($\{BW_{11}\}$) and gly.

Fig. S2 The PXRD patterns of **1**–**6**.

Fig. S3 The 3-D supramolecular architecture of **1** constructed by hydrogen-bonding interactions. The pink bonds highlight the hydrogen-bond interactions.

Fig. S4 The 3-D structure of **1**. KO_6 = pink octahedral.

Fig. S5 Two $\{K_4\}$ arms linked to the $\{Ce_2(gly)_4\}$ unit forming a $\{K_8Ce_2(gly)_4\}$ cluster in the 3-D structure of **1**. KO_6 = pink octahedral.

Fig. S6 The solid-state emission spectrum of of $K_8[\alpha\text{-}BW_{11}O_{39}H]\cdot 13H_2O$ taken by monitoring the emission at 1059 nm as **3**.

Fig. S7 The solid-state emission spectrum of of $K_8[\alpha\text{-}BW_{11}O_{39}H]\cdot 13H_2O$ taken by monitoring the emission at 597 nm as **4**.

Fig. S8 The luminescence decay curve of $K_8[\alpha\text{-}BW_{11}O_{39}H]\cdot 13H_2O$ taken by monitoring the emission at 597 nm.

Fig. S9 The luminescence quantum yield measurement (Φ) of **4** at ambient temperature under excitation at 403 nm.

Fig. S10 The luminescence quantum yield measurement (Φ) of $K_8[\alpha\text{-}BW_{11}O_{39}H]\cdot 13H_2O$ at ambient temperature under excitation at 403 nm.

Fig. S11 The solid-state emission spectrum of of $K_8[\alpha\text{-}BW_{11}O_{39}H]\cdot 13H_2O$ taken by monitoring the emission at 614 nm as **5**.

Fig. S12 The luminescence decay curve of $K_8[BW_{11}O_{39}H]\cdot 13H_2O$ taken by monitoring the emission at 614 nm.

Fig. S13 The luminescence quantum yield measurement (Φ) of **4** at ambient temperature under excitation at 395 nm.

Fig. S14 The luminescence quantum yield measurement (Φ) of $K_8[\alpha\text{-}BW_{11}O_{39}H]\cdot 13H_2O$ at ambient temperature under excitation at 395 nm.

Fig. S15 CIE diagram of the emissions of **4** and **5**.

Fig. S16 (a) The TG curves of **1**–**6**. (b) The PXRD patterns of **3** at variable temperatures. (c) The IR spectra of **3** at variable temperatures

Fig. S17 The color changes of **3** at different temperatures.

Table S1. Bond valence sum (BVS) calculations of all the W, B and Ln atoms in **1**–**6**.

Table S2. The luminescence lifetimes of **3**–**5** by monitoring at the corresponding strongest emissions and the luminescence lifetimes of BW_{11} ($K_8[BW_{11}O_{39}H]\cdot 13H_2O$) monitoring at 597 and 614 nm, respectively.

The structural refinement details in 1-6:

Thanks to the large structures of **1-6** and the existence of a large amount of weight atoms, their intensity data are not very good, leading to the ADP max/min ratio of some atoms, and it is very difficult to refine these large structures, therefore, some unit-occupancy atoms have been refined isotropically and restrainedly refined.

For **1**: The ISOR instruction is used for O6, O23, O28, O33, O38, O42, C2, O41, O1, O39, O1W, O21, O17, O4, O9, O43, C3, O36, O25, O13, O10W, O15, O8, O7, O14, B1, O10, O24, O28 and O34. O6W-O9W, O11W-O14W and O3 are refined isostropicallly. 674 parameters and 180 restraints are used in the refinement.

For **2**: The ISOR instruction is used for C3, O10, O31, O6, O26, C2 and B1. O6W-O9W and O11W-O14W are refined isostropicallly. 680 parameters and 42 restraints are used in the refinement.

For **3**: The ISOR instruction is used for O29, N1, C2, O1W, O35, O30, O13W, O29, O26, N1, C1, B1, O14 and O6. O8W-O9W, O11W, O12W and O14W are refined isostropicallly. 697 parameters and 84 restraints are used in the refinement.

For **4**: The ISOR instruction is used for O14, B1, N2, O14, O12, O13W, O3, O43, O23, O1, and Na1. O8W-O9W, O11W, O12W and O14W are refined isostropicallly. 692 parameters and 66 restraints are used in the refinement.

For **5**: The ISOR instruction is used for O23, O31, O33 and B1. O6W-O9W and O11W-O14W are refined isostropicallly. 681 parameters and 24 restraints are used in the refinement.

For **6**: The ISOR instruction is used for C3, O22, O9, O19 and B1. O6W-O9W and O11W-O14W are refined isostropicallly. The DFIX instruction is used for N2 and C4. 682 parameters and 31 restraints are used in the refinement.

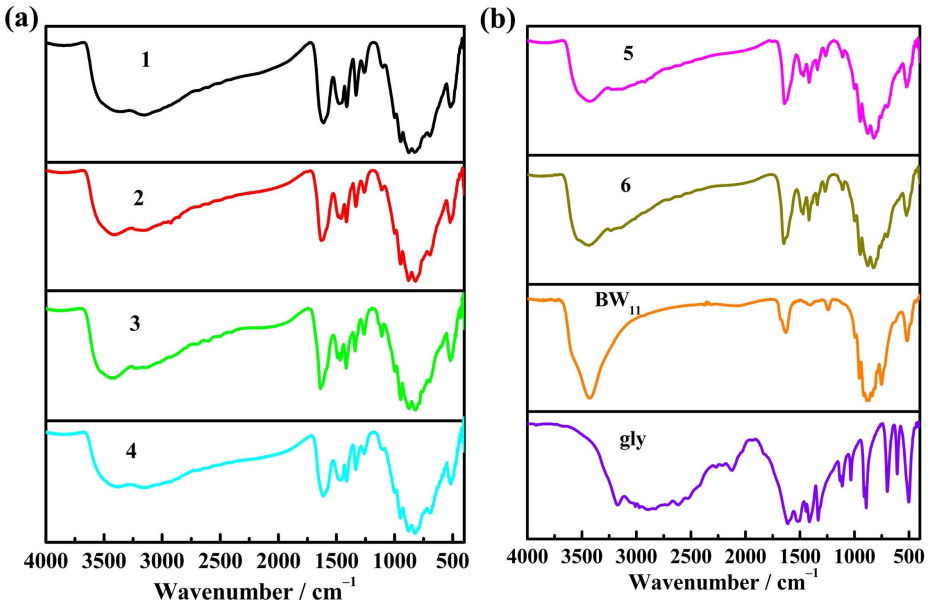

Fig. S1 IR spectra of **1**–**6**, $K_8[\alpha\text{-}BW_{11}O_{39}H]\cdot 13H_2O$ ($\{BW_{11}\}$) and gly.

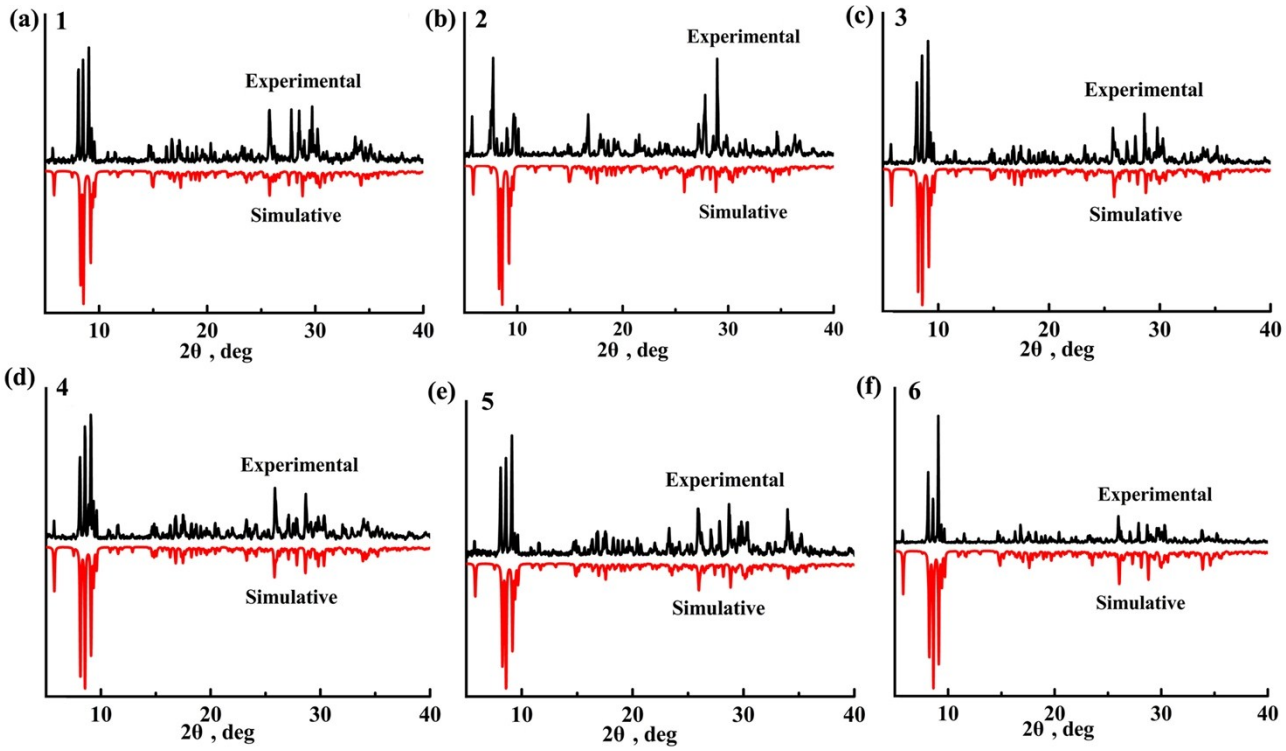

Fig. S2 The experimental and simulative PXRD patterns of **1**–**6**.

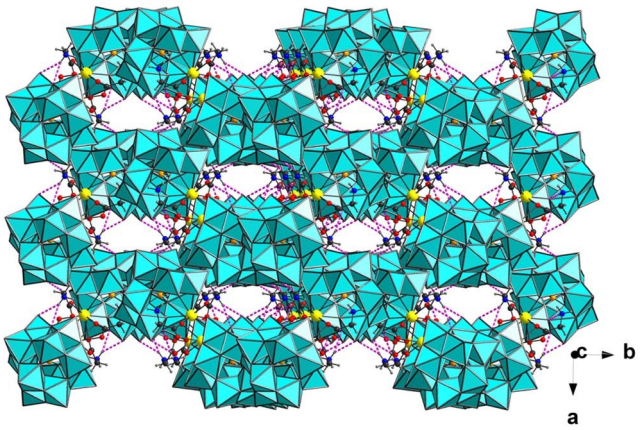

Fig. S3 The 3-D supramolecular architecture of **1** constructed by hydrogen-bonding interactions. The pink bonds highlight the hydrogen-bond interactions.

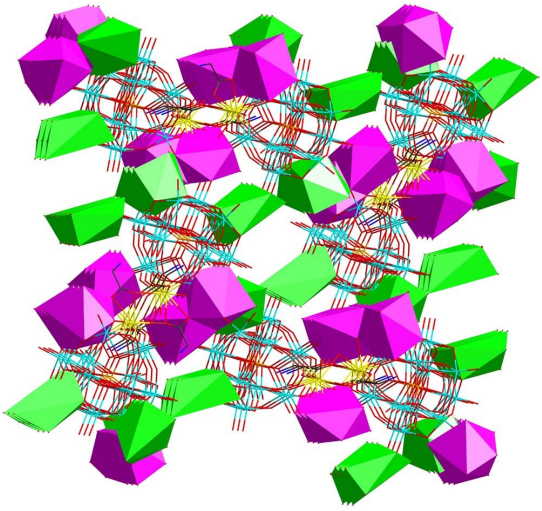

Fig. S4 The 3-D structure of **1**. KO_6 = pink octahedral, $\{NaO_6\}$ and $\{NaO_7\}$: bright green.

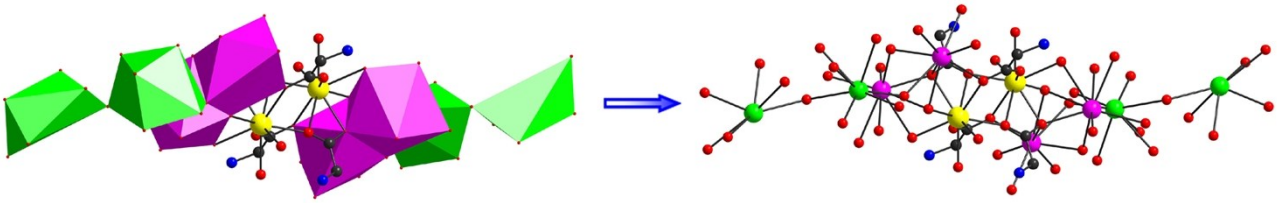

Fig. S5 Two $\{K_2Na_2\}$ arms linked to the $\{Ce_2(gly)_4\}$ unit forming a $\{K_4Na_4Ce_2(gly)_4\}$ cluster in the 3-D structure of **1**. KO_6 = pink octahedral, $\{NaO_6\}$ and $\{NaO_7\}$: bright green.

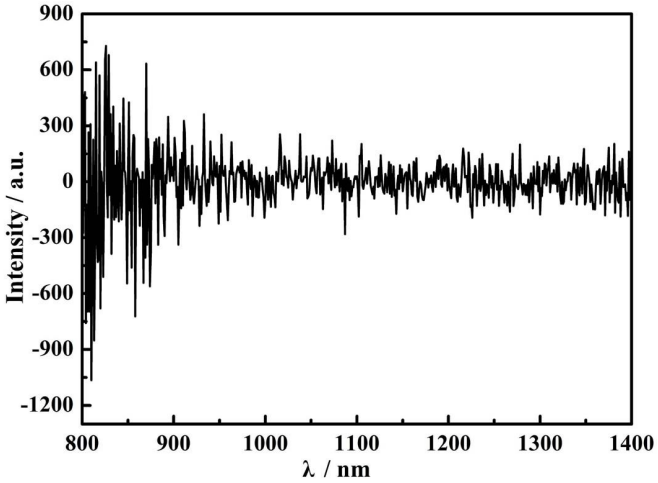

Fig. S6 The solid-state emission spectrum of of $K_8[\alpha\text{-}BW_{11}O_{39}H]\cdot 13H_2O$ taken by monitoring the emission at 1059 nm as **3**.

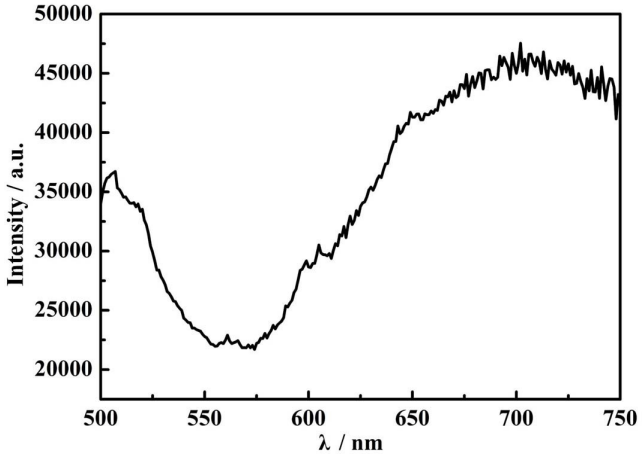

Fig. S7 The solid-state emission spectrum of of $K_8[\alpha\text{-}BW_{11}O_{39}H]\cdot 13H_2O$ taken by monitoring the emission at 597 nm as **4**.

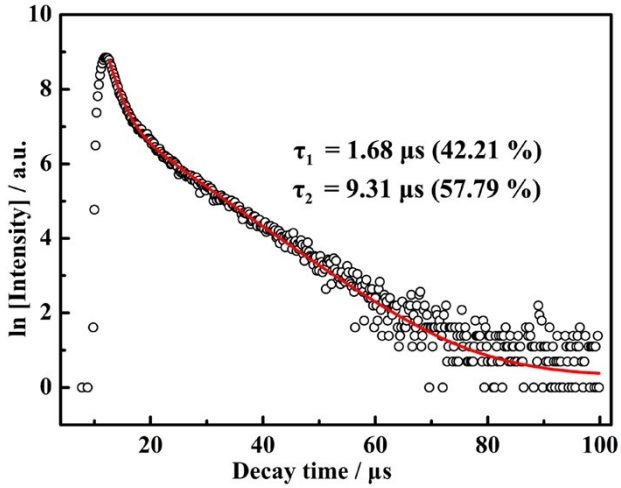

Fig. S8 The luminescence decay curve of $K_8[\alpha\text{-}BW_{11}O_{39}H]\cdot 13H_2O$ taken by monitoring the emission at 597 nm.

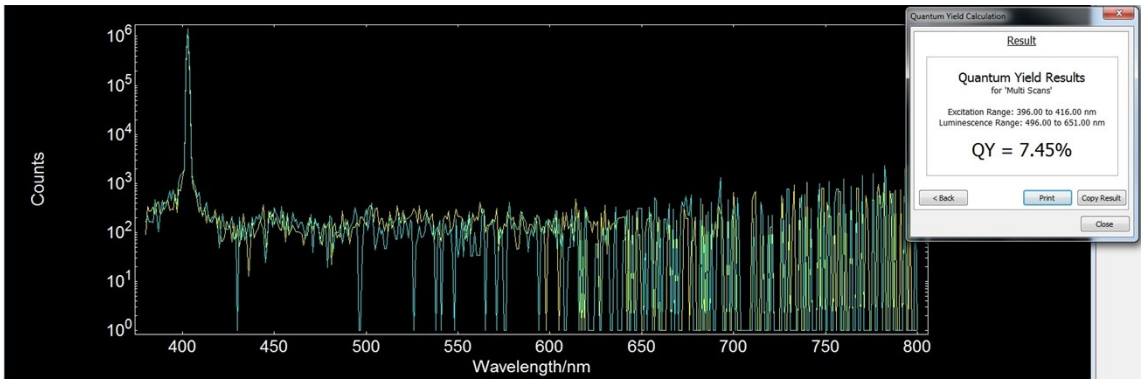

Fig. S9 The luminescence quantum yield measurement (Φ) of **4** at ambient temperature under excitation at 403 nm.

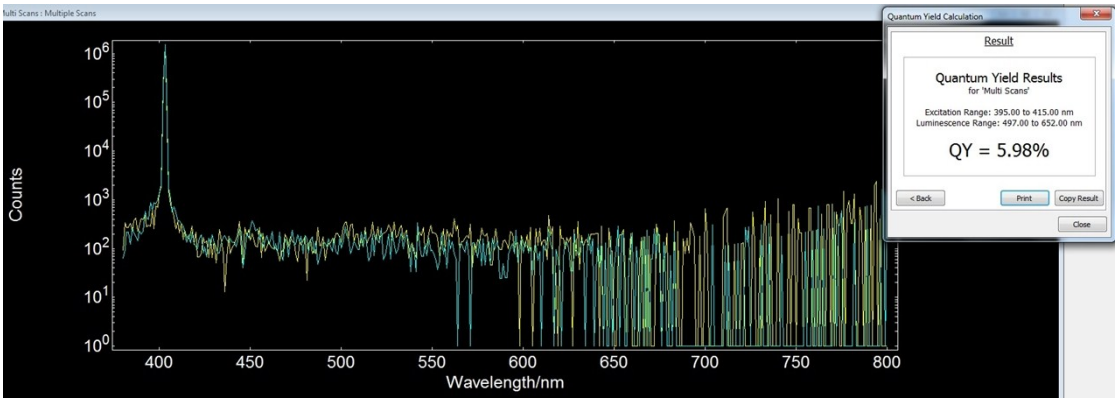

Fig. S10 The luminescence quantum yield measurement (Φ) of $K_8[\alpha\text{-}BW_{11}O_{39}H]\cdot 13H_2O$ at ambient temperature under excitation at 403 nm.

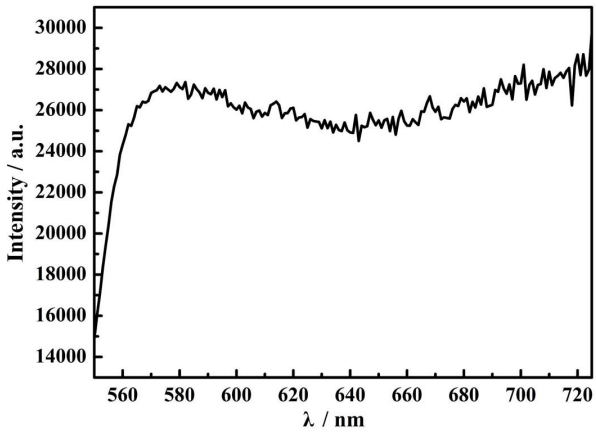

Fig. S11 The solid-state emission spectrum of of $K_8[\alpha\text{-}BW_{11}O_{39}H]\cdot 13H_2O$ taken by monitoring the emission at 614 nm as **5**.

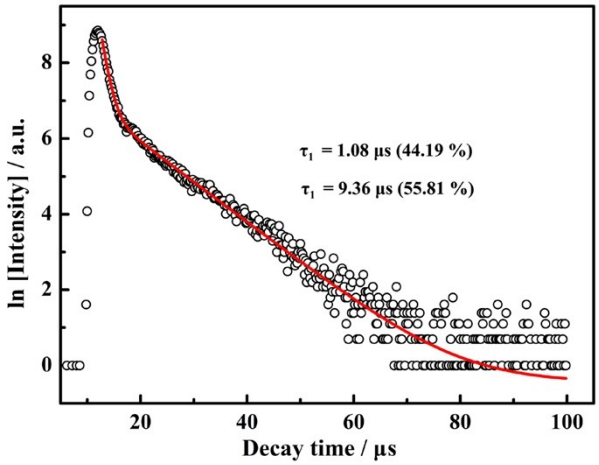

Fig. S12 The luminescence decay curve of $K_8[\alpha\text{-}BW_{11}O_{39}H]\cdot 13H_2O$ taken by monitoring the emission at 614 nm.

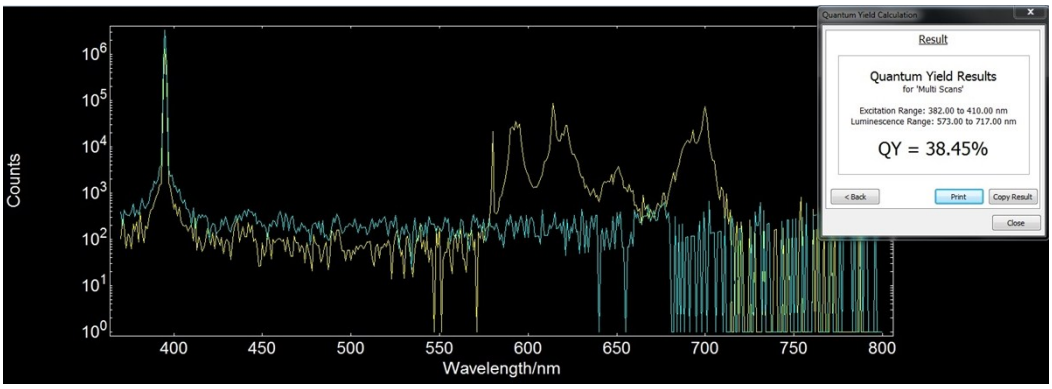

Fig. S13 The luminescence quantum yield measurement (Φ) of **4** at ambient temperature under excitation at 395 nm.

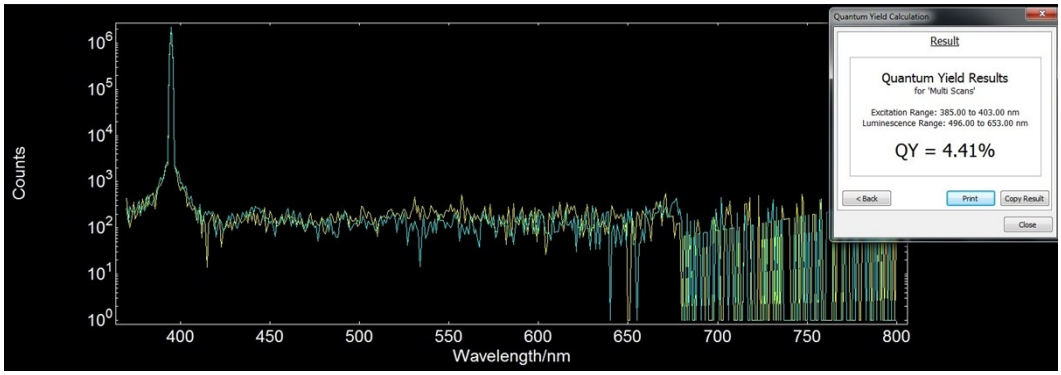

Fig. S14 The luminescence quantum yield measurement (Φ) of $K_8[\alpha\text{-}BW_{11}O_{39}H]\cdot 13H_2O$ at ambient temperature under excitation at 395 nm.

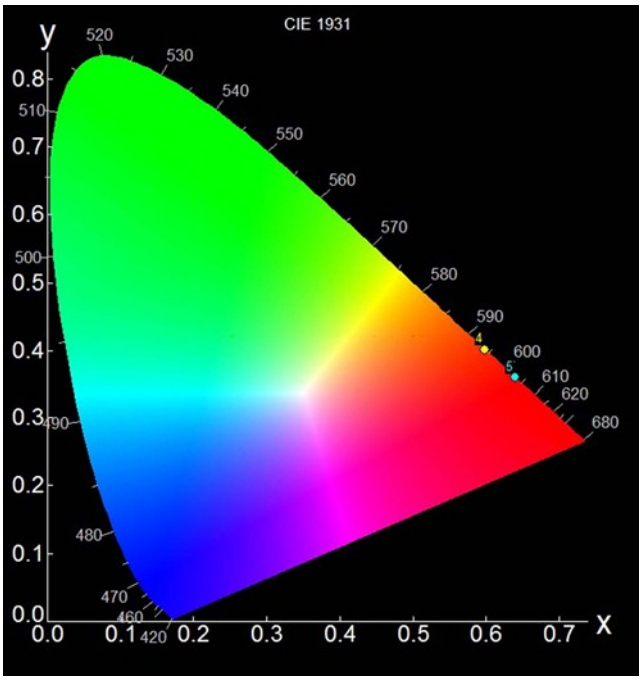

Fig. S15 CIE diagram of the emissions of 4 and 5.

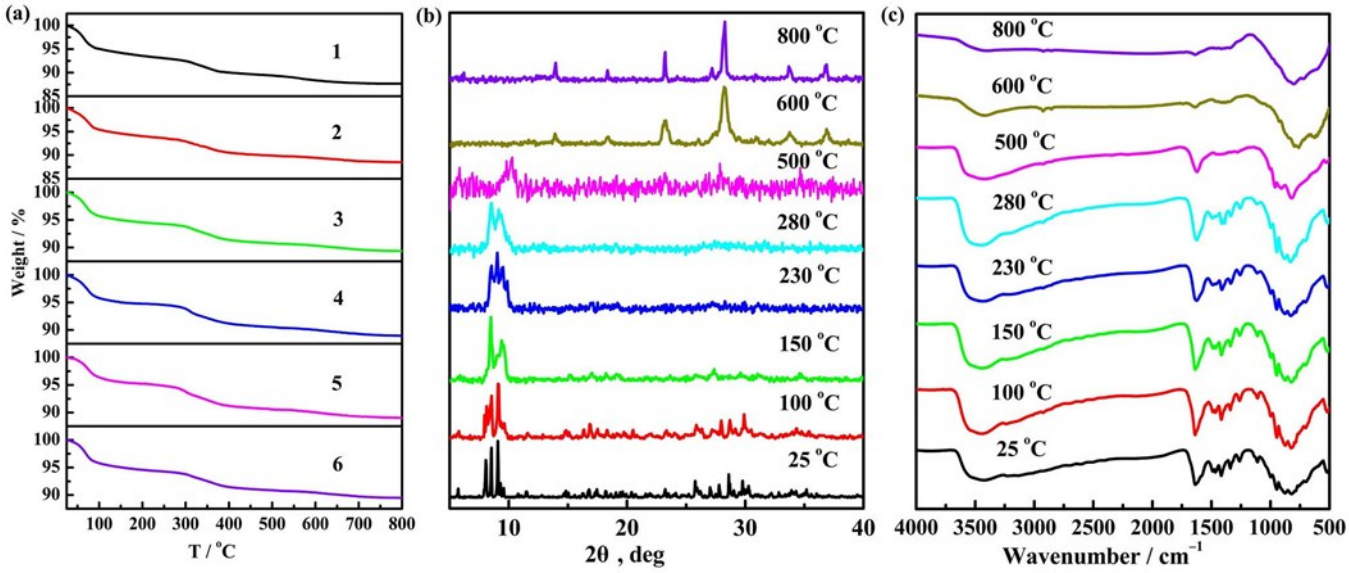

Fig. S16 (a) The TG curves of **1**–**6**. (b) The PXRD patterns of **3** at variable temperatures. (c) The IR spectra of **3** at variable temperatures.

TG Analyses

In order to investigate the thermal stability of **1**–**6**, their TG measurements were conducted in the flowing N_2 atmosphere with a heating rate of 10 °C min^{-1} in the temperature range of 25–800 °C (Fig. S16a). As for **1**–**6**, the TG curves undergo the similar two-step weight loss from 25 to 800 °C. The first weight loss of 6.83% (calcd. 6.31%) from 25 to 248 °C for **1**, 6.45% (calcd. 6.31%) from 25 to 258 °C for **2**, 5.97% (calcd. 6.30%) from 25 to 256 °C for **3**, 5.88% (calcd. 6.29%) from 25 to 257 °C for **4**, 5.99% (calcd. 6.29%) from 25 to 267 °C for **5**, 5.82% (calcd. 6.25%) from 25 to 258 °C for **6** is attributable to the liberation of 23 lattice water molecules. A further

heating to 800 °C leads to the second weight loss of 5.44% (calcd. 5.12%) for **1**, 5.10% (calcd. 5.12%) for **2**, 4.72% (calcd. 5.12%) for **3**, 5.36% (calcd. 5.11%) for **4**, 5.07% (calcd. 5.10%) for **5**, 4.85% (calcd. 5.08%) for **6**, corresponding to the decomposition of four gly ligands and the dehydration of four protons.

For a better understanding the thermal decomposition process, a combination of variable-temperature IR spectra, variable-temperature PXRD patterns and TG analyses was applied. Considering that the TG curves of **1**–**6** go through the same evolutional trend, the variable-temperature IR spectra and variable-temperature PXRD patterns of 3 were studied as a representative. As can be seen from Fig. S16b,c, the PXRD pattern at 100 °C is similar to that recorded at room temperature, suggesting that the polyoxoanionic skeleton of **3** is stable at this temperature range in spite of the departure of partial lattice water molecules, which is also supported by the good agreement of the IR spectra at 100 °C and 25°C. Besides, when the temperature is heated to 100 °C, **3** does not show obvious color change (Fig. S17), further affirming the conjecture that only partial lattice water molecules are released. The slight differences of PXRD patterns between 100 and 280 °C at low 2θ angles along with several peaks of the PXRD patterns at high 2θ angles gradually fading out are mainly due to the removal of all the lattice water molecules. As we know, the loss of all the lattice water molecules will lead to the efflorescence of the crystalline sample, and thus makes the PXRD patterns become worse at 280 °C. However, the characteristic peaks derived from the polyoxoanionic skeleton in the low diffraction angles still exist, indicating that the basic framework is still maintained, which is consolidated by the coherence of the IR spectrum at 280 °C with that at 25 °C. This result is in excellent accordance with the first weight loss of 23 water molecules in the TG curve. As the temperature arises to 500 °C, the characteristic peaks in the PXRD spectrum still persists but give way to a broad peak and shift to a larger 2θ value, implying that the polyoxoanionic framework at this temperature was at least partially decomposed, and this speculation is certified by the fast coloration change from pale purple to black presumably resulted from the carbonization of gly ingredients and the obvious changes in the IR spectrum, in which not only the ν(C–N) and ν(C=O) vibration bands gradually disappear, but also the ν(W–O_t), ν(B–O), ν(W–O_b) and ν(W–O_c) vibration peaks become slender. The PXRD pattern at 600 °C is clearly different from the abovementioned PXRD patterns and ν(C–N) and ν(C=O) vibration bands in the IR spectrum have vanished, illustrating the release of gly components. After 600 °C, a new phase emerges as some new diffraction peaks in the PXRD pattern turns up between 600 and 800 °C, which is demonstrated by the TG curve of the dehydration of protons resulting in the gradual decomposition of the main polyoxoanionic skeleton, as well as the pale yellow-green color of **3** at 800 °C (Fig. S17).

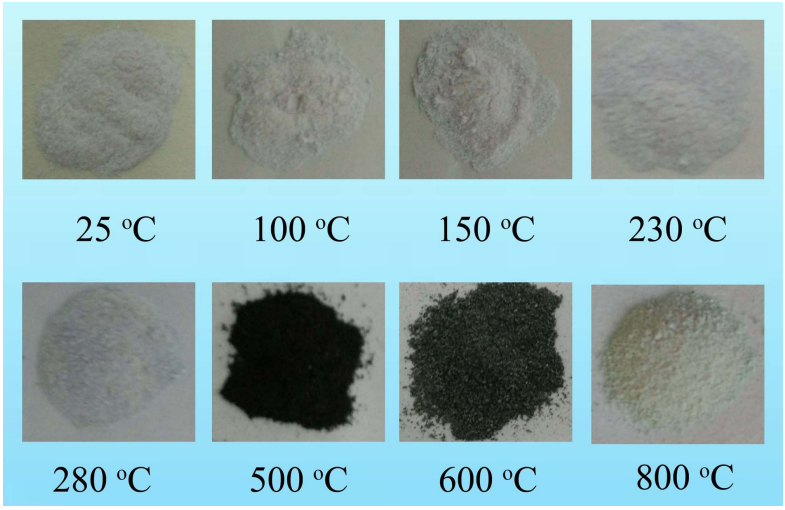

Fig. S17 The color changes of **3** at different temperatures.

Table S1. Bond valence sum (BVS) calculations of all the W, B and Ln atoms in **1–6**.

Atom	BVS(**1**)	BVS(**2**)	BVS(**3**)	BVS(**4**)	BVS(**5**)	BVS(**6**)
Ln	3.065	3.481	3.232	3.130	3.352	2.790
B	2.741	2.819	2.786	2.714	2.785	2.792
W1	6.171	6.233	6.209	6.141	6.374	6.032
W2	6.438	6.159	6.333	6.339	6.018	6.212
W3	6.296	6.084	6.156	6.264	6.099	6.441
W4	6.237	6.135	6.162	6.116	6.208	6.194
W5	6.242	6.098	6.316	6.316	6.244	6.224
W6	6.276	6.147	6.281	6.208	6.214	6.195
W7	6.290	6.277	6.324	6.362	6.192	6.178
W8	6.300	6.146	6.251	6.059	6.144	6.222
W9	6.047	6.281	6.106	6.177	6.216	6.207
W10	6.300	6.205	6.082	6.194	6.144	5.965
W11	6.107	6.043	6.153	6.308	6.056	6.072

Table S2. The luminescence lifetimes of **3–5** by monitoring at the corresponding strongest emissions and the luminescence lifetimes of BW_{11} monitoring at 597 and 614 nm, respectively.

Compounds	τ_1/μs	A_1	Percentage /%	τ_2/μs	A_2	Percentage /%	τ/μs
3	0.96	4267.15	17.91	9.99	1886.99	82.09	8.38
4	3.95	3695.66	50.12	9.00	1614.87	49.88	6.47
5	1785.25	4954.38	100.00				
BW_{11} (597 nm)	1.68	5781.97	42.21	9.31	1429.36	57.79	6.09
BW_{11} (614 nm)	1.08	5622.87	44.19	9.36	819.84	55.81	5.70